Modeling of flat-sheet and spiral-wound nanofiltration configurations and its application in seawater nanofiltration

Citation: Roy, Yagnaseni, Mostafa H. Sharqawy, and John H. Lienhard. “Modeling of Flat-Sheet and Spiral-Wound Nanofiltration Configurations and Its Application in Seawater Nanofiltration.” Journal of Membrane Science 493 (November 2015): 360–372.

As Published: http://dx.doi.org/10.1016/j.memsci.2015.06.030

Publisher: Elsevier

Persistent URL: http://hdl.handle.net/1721.1/99918

Version: Author's final manuscript: final author's manuscript post peer review, without publisher's formatting or copy editing

This pre-print corresponds to the following article:Y. Roy, M.H. Sharqawy, and J.H. Lienhard V, “Modeling of Flat-Sheet and Spiral-Wound Nanofiltration Configurations and Its Application in Seawater Nanofiltration,” *J. Membrane Sci.*, **493**:630-642, 1 Nov. 2015. '

Modeling of Flat-Sheet and Spiral-Wound Nanofiltration Configurations and Its Application in Seawater Nanofiltration

Yagnaseni Roy[1], Mostafa H. Sharqawy[2], John H. Lienhard V[*, 1]

[1] Department of Mechanical Engineering, Massachusetts Institute of Technology, Cambridge, MA 02139-4307, USA
[2] Department of Mechanical Engineering, King Fahd University of Petroleum and Minerals, Dhahran 31261, Saudi Arabia

Abstract

The Donnan Steric Pore Model with dielectric exclusion (DSPM-DE) is implemented over flat-sheet and spiral-wound leaves to develop a comprehensive model for nanofiltration modules. This model allows the user to gain insight into the physics of the nanofiltration process by allowing one to adjust and investigate effects of membrane charge, pore radius, and other membrane characteristics. The study shows how operating conditions such as feed flow rate and pressure affect the recovery ratio and solute rejection across the membrane. A comparison is made between the results for the flat-sheet and spiral-wound configurations. The comparison showed that for the spiral-wound leaf, the maximum values of transmembrane pressure, flux and velocity occur at the feed entrance (near the permeate exit), and the lowest value of these quantities are at the diametrically opposite corner. This is in contrast to the flat-sheet leaf, where all the quantities vary only in the feed flow direction. However it is found that the extent of variation of these quantities along the permeate flow direction in the spiral-wound membrane is negligibly small in most cases. Also, for identical geometries and operating conditions, the flat-sheet and spiral-wound configurations give similar results. Thus the computationally expensive and complex spiral-wound model can be replaced by the flat-sheet model for a variety of purposes. In addition, the model was utilized to predict the performance of a seawater nanofiltration system which has been validated with the data obtained from a large-scale seawater desalination plant, thereby establishing a reliable model for desalination using nanofiltration.

Keywords

---

[*] Corresponding author
Email address: lienhard@mit.edu (John H. Lienhard V), Tel. +1 617-253-1000

Nanofiltration, Flat sheet, Spiral wound, Seawater, Modeling

Nomenclature

A_k	porosity of membrane	
C	concentration	mol m^{-3}
C_X	membrane volumetric charge density	mol m^{-3}
dS	contact area between channel and membrane in each cell	m^2
D	solute diffusivity	m^2 s^{-1}
D_H	hydraulic diameter of feed channel	m
e_0	electronic charge (1.602×10^{-19} C)	C
f	friction coefficient	
F	Faraday's constant	C eq^{-1}
G	Gibbs free energy	J
i_v	Van 't Hoff coefficient	
I	ionic strength	mol L^{-1}
h	channel height	m
j	solute flux	mol $m^{-2}s^{-1}$
J_w	solvent permeation flux	m s^{-1}
k	mass transfer coefficient in feed channel	m s^{-1}
k_B	Boltzmann constant (1.380648×10^{-23} J K^{-1})	J K^{-1}
K	hindrance factor	
l	distance along the feed channel	m
L	membrane length	m
L_{mix}	mixing length of spacer	m
$\dot{m}$	mass flow rate	mol s^{-1}
N_A	Avogadro number (6.022141×10^{23} mol^{-1})	mol^{-1}
P	pressure	Pa
ΔP_{net}	net driving pressure	Pa
ΔP_{loss}	hydraulic pressure loss along feed channel	Pa
Q	flow rate	m^3 s^{-1}
r_i	Stokes radius of solute	m
r_{pore}	pore radius of membrane	m
R	universal gas constant	J mol^{-1} K^{-1}
T	temperature	K
u	Velocity	m s^{-1}
W	membrane width	m
x	distance normal to membrane	m
Δx	membrane active layer thickness	m
z	valence of species	

Greek symbols

γ	activity coefficient	
ε_0	absolute permittivity of vacuum (8.854×10^{-12} Fm^{-1})	F m^{-1}
ε	dielectric constant of medium	
ζ	potential gradient at feed-membrane interface	V m^{-1}
η	mixing efficiency of spacer	
λ	ratio of solute Stokes radius to pore radius	
ν	kinematic viscosity	m s^{-1}
π	osmotic pressure	N m^{-2}
ρ	density	kg m^{-3}
Φ_i	steric partitioning factor	
Φ_B	Born solvation factor for partitioning	
ψ	membrane potential	V

Subscripts

c	Convective
d	Diffusive
D	Donnan potential
f	feed bulk
i	solute species
in	Inlet
m	feed-membrane interface
out	Outlet
p	permeate just outside the membrane
$pore$	inside pore
w	Solvent
∞	Bulk

Dimensionless Parameters

Pe	Peclet number	$\frac{2h_f u_w}{D_\infty}$
Re	Reynolds number	$\frac{u_w D_H}{\nu}$
Sc	Schmidt number	$\frac{\nu}{D_\infty}$

1. Introduction

Nanofiltration (NF) is a pressure driven membrane-based water purification process with performance between that of reverse osmosis (RO) and ultrafiltration (UF) [1], [2]. The interplay of three exclusion mechanisms, the steric effects, Donnan exclusion effects and dielectric effects allow a great degree of variability in membrane selectivity [2], [3], [4], [5]. In general, nanofiltration shows high rejection of divalent and multivalent ions [6], [7], [8]. It created a revolution in the world of separation technology, previously dominated by RO, due to its high water permeability and hence lower energy consumption in addition to its ion selectivity [2], [9]. In its early days, nanofiltration was utilized predominantly in the dairy and chemical industries applications [9]. In more recent years, it has been used in a variety of applications such as desalination [2] [8], wastewater treatment [10], diafiltration [11], petroleum fractionation [12], and treatment of mining water [13].

The Donnan Steric Pore Model with dielectric exclusion (DSPM-DE) is a comprehensive model of the mechanism of nanofiltration. This model solves the Extended Nernst Planck equation (ENP) for each solute species through the membrane and uses boundary conditions at the membrane surfaces to account for the Donnan exclusion, dielectric exclusion, and steric exclusion effects. It is an improvement upon the original Donnan Steric Pore Model (DSPM) [1] [3] [11] [14], as it explains the mechanism of dielectric exclusion, which is vital for the correct prediction of the rejection of multivalent ions by the nanofiltration membrane. In the current work, the dielectric exclusion mechanism based on the Born effect is considered. The Born effect accounts for the energy barrier for solvation inside the pores and hence decreased dielectric constant of the solvent [3] [15] [16]. According to the work of Bowen et al [3], this mechanism of dielectric exclusion is dominant over the other effect used to explain dielectric exclusion, involving image charges that develop at the interface of the bulk solution and membrane (as described by Bandini et al [5]), for most nanofiltration conditions. This is explained by the fact that the small pores in nanofiltration membranes cause the value of the dielectric constant of the solvent inside the membrane to approach that of the membrane itself and moreover, the image charges are screened in electrolyte solutions due to the formation of electrical double layers [3]. The DSPM-DE model using the Born effect for dielectric exclusion has been well validated with lab-scale experiments [4].

Geraldes *et al.* [4] introduced the software 'Nanofiltran' that solves the discretized and linearized ENP equations. Nanofiltran is a robust and comprehensive software that considers the non-ideality of solutions and the concentration polarization effect at the feed-side of the membrane. However, it models a 'small patch' of membrane and does not account for the streamwise distribution of various quantities, namely flow parameters such as cross-flow velocities, solute concentrations, and transmembrane flux as well as solute rejection profiles along a large membrane leaf. Thus 'Nanofiltran' cannot be used to describe large membranes that are used in large-scale nanofiltration units.

Hitherto, to the best knowledge of the authors, a comprehensive model of a spiral-wound module of nanofiltration that accounts for the detailed mechanism of nanofiltration has not been introduced. Schwinge *et al.* [17] showed a detailed analysis of spiral wound membranes and the spatial distribution of quantities such as transmembrane flux, transmembrane pressure difference, feed concentration, and crossflow velocity along the membrane. This study, however, is general and can be applied to reverse osmosis, nanofiltration, ultrafiltration, or microfiltration membranes. A complete study of nanofiltration membranes demands attention not only to the general features of the membrane, but also to its unique separation capability and mechanism. A comprehensive study of nanofiltration mechanism involves a combination of the diffusive transport, electro-migration and convective transport through narrow pores, therefore requiring use of the Extended Nernst-Planck equation, modified by the hindered transport theory [3], [4], [5].

The NF model introduced in the present work is based on the DSPM-DE model, applied over a flat-sheet and spiral-wound leaf. The results from the individual leaves can be easily treated as if in a parallel connection to depict a spiral-wound element, which may in turn be put into a train of spiral-wound elements that exist in series within a pressure vessel. The user can make use of several degrees of freedom in the definition of the membrane, namely the membrane pore radius, membrane effective thickness, membrane charge, pore dielectric constant and membrane dimensions. It is also possible to test the behavior of individual leaves or an individual element for different feed flow rates, compositions, and transmembrane pressures. Various feed water properties, such as pH levels and temperature can be incorporated into the model by characterizing the membrane and subsequently using these parameters in the model [14].

Another important aim of this work is to provide results for each constituent ion of seawater from its nanofiltration modeling. Most commonly, seawater is modeled by a sodium-chloride solution at a concentration similar to that of seawater [18]. While this is a reasonable approximation for seawater [19] [20], it does not give any information about the permeate concentrations of the many individual ions in seawater. Thus, it fails to provide essential information regarding concentration of scale-causing ions such as magnesium, calcium, sulphate and carbonate ions that enter thermal desalination processes for which nanofiltration is used as a pretreatment [21].

The use of nanofiltration as a pretreatment stage in thermal desalination processes, namely, Multi-Stage Flash (MSF) and Multi-Effect-Distillation (MED) seawater desalination plants, in order to increase the top brine temperature (TBT), has been a subject of interest and study by several researchers [13], [21], [22], [23]. Nanofiltration efficiently removes scale-causing ions such as calcium, magnesium, sulphate, and carbonate ions and hence adds potential to increase the top brine temperature (TBT) in an MSF or MED plant. In reference [21], the Saline Water Conversion Corporation, Research and Development Center (SWCC-RDC) demonstrated that the addition of a nanofiltration unit as pretreatment to MSF was found to be successful in the removal of turbidity, residual bacteria, and seawater total dissolved solids (TDS). Moreover, since it resulted in lower concentrations of the scale forming constituents, the TBT could be increased up to 160^{o}C [21]. Consequently, it reduced the thermal energy input and decreased the antiscalant additives, as evident from experimental results of a pilot plant. Several experimental efforts have been made on nanofiltration of seawater, both at lab scale as well as in desalination plants [23], [24], [25]. However, the aim of this work is to provide a useful model to reduce the number of experiments required for such studies.

In summary, this work aims at introducing a comprehensive model for flat-sheet and spiral-wound nanofiltration membranes and evaluates their performance for the seawater desalination application. A model is introduced for analyzing commercially used nanofiltration elements that allows the user to understand the mechanism of filtration and provides the flexibility to simulate a wide range of membrane types by adjusting the various key parameters that characterize the membrane. Further, a detailed analysis of seawater nanofiltration using this model is described.

2. Mathematical Model

The model presented in this work is an integrated version of the previously developed DSPM-DE model [4]. In this work, the elemental equations of that model are 'threaded together' to simulate the transport over a large membrane leaf with locally varying conditions. The large membrane leaf is divided into cells and the DSPM-DE model equations are applied by moving from one cell to another while accounting for the mass conservation of each solute species and of the solvent. In addition, the hydraulic pressure losses along the feed flow direction in the feed channel are considered. Figure 1a and 1b are schematic diagrams of the flat-sheet membrane leaf and the spiral-wound membrane leaf configurations respectively. The two configurations differ by the flow arrangement. Figure 1a shows the flat-sheet membrane configuration with the feed and permeate flows in their respective channels, flowing parallel to one-another. The membrane leaf has a width W and a length L along the feed flow direction. As shown, the cells have a width equal to that of the membrane leaf and they split the length of the membrane into several segments. Figure 1b shows an unwound spiral-wound membrane leaf. In this configuration, the feed and permeate flow perpendicular to each-other in their respective channels. Therefore, in order to capture the variation of the flow parameters and the rejection performance of the membrane in both the longitudinal and transverse directions, the cells are square elements that split both the width and length of the membrane into segments. Grid independence studies of the present work have showed that beyond 100 cells (in the feed flow direction for the flat-sheet case and 100 cells each in the feed and permeate flow directions in the spiral-wound case), the computational results vary by less than 1%. Therefore, 100 cells were taken for all cases in the present work.

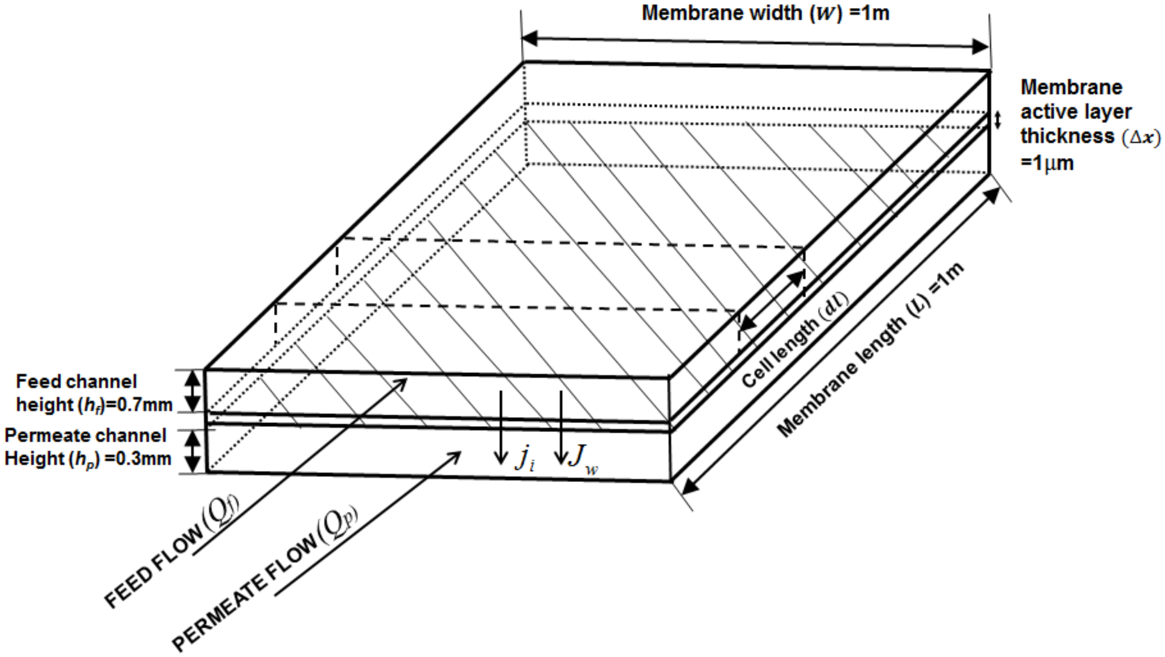

(a)

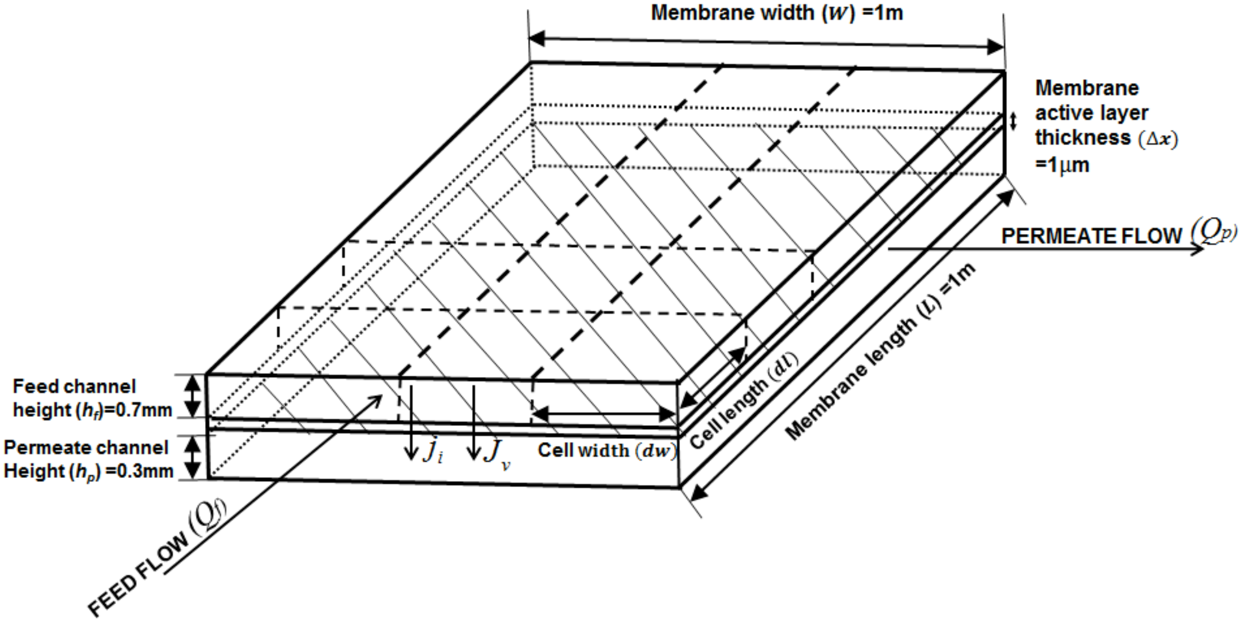

(b)

Fig. 1 Schematic diagrams of (a) flat-sheet membrane, and (b) unwound spiral-wound leaf.

2.1. Governing Equations

The Extended Nernst-Planck equation (ENP) describes the transfer of ions under the influence of concentration gradient, electric field, and inertia forces. For each solute $'i'$ transferring through the membrane pores, the ENP equation is given by Eq. (1).

$$j_{i,pore} = -D_{i,pore}\frac{dC_{i,pore}}{dx} - \frac{z_i C_{i,pore} D_{i,pore}}{RT} F \frac{d\psi}{dx} + K_{i,c} C_{i,pore} J_w \qquad (1)$$

where $j_{i,pore}$ is the flux of the species $'i'$ inside a pore*,* the first term on the right represents the transport due to diffusion (concentration gradient), the second term represents the transport due to electric field (potential gradient), and the last term represents the transport due to convective forces. Due to the extremely small pore sizes in nanofiltration membranes, the transport of the solute is 'hindered'. Thus, the ENP has been modified by the hindered transport theory [26] [27] through introduction of the coefficients $K_{i,c}, K_{i,d}$ which give a measure of the 'lag' of a spherical solute moving inside a cylindrical pore and the enhanced drag experienced by the solute respectively. Both these coefficients are functions of the ratio of solute radius to pore radius, λ_i [3].

The diffusivity (diffusion coefficient) of the solute inside the pore is related to the diffusivity of the solute in the bulk solution as given by Eq. (2):

$$D_{i,pore} = K_{i,d} D_{i,\infty} \qquad (2)$$

For $\lambda_i \leq 0.95$, [4]

$$K_{i,d} = \left(\frac{\begin{array}{c} 1+(9/8)\lambda_i \ln\lambda_i - 1.56034\lambda_i + 0.528155\lambda_i^2 + 1.91521\lambda_i^3 \\ -2.81903\lambda_i^4 + 0.270788\lambda_i^5 - 1.10115\lambda_i^6 - 0.435933\lambda_i^7 \end{array}}{\Phi_i} \right) \tag{3}$$

and for $\lambda_i > 0.95$, [4]

$$K_{i,d} = 0.984\left(\frac{1-\lambda_i}{\lambda_i}\right)^{5/2} \tag{4}$$

For convection, the hindrance factor is [4]

$$K_{i,c} = \left(\frac{1+3.867\lambda_1 - 1.907\lambda_i^2 - 0.834\lambda_i^3}{1+1.867\lambda_i - 0.741\lambda_i^2}\right) \tag{5}$$

The equilibrium boundary condition at the membrane-feed solution interface due to the combination of the steric, Donnan and dielectric effects is given by

$$\frac{\gamma_{i,pore}C_{i,pore}}{\gamma_{i,m}C_{i,m}} = \Phi_i \Phi_B \exp\left(-\frac{z_i F}{RT}\Delta\psi_{D,m}\right)\bigg|_{in} \tag{6}$$

It is to be noted that $C_{i,pore}$ in equation (6) is the solute concentration just within the pore 'entrance'. This is important because the solute concentration varies along the pore. $C_{i,m}$ is the feed concentration at the membrane-feed solution interface. $\gamma_{i,pore}, \gamma_{i,m}$ are solute activity coefficients just within the pore entrance and at the membrane and feed solution interface respectively; Φ_i, Φ_B are the steric partitioning factor and solvation energy contribution to partitioning respectively, and $\Delta\psi_{D,m}$ is the Donnan potential on the feed side, which is the potential difference between the point just within the pore entrance and the solution at the feed-membrane interface [4].

Furthermore, the steric partitioning factor is given by [4]

$$\Phi_i = (1-\lambda_i)^2\text{, where } \lambda_i = \frac{r_i}{r_{pore}} \tag{7}$$

The Born solvation energy contribution to partitioning is given by [4]

$$\Phi_B = \left(\frac{-\Delta G_i}{k_B T}\right) \tag{8}$$

where ΔG is the Gibbs free energy of solvation given by [4]

$$\Delta G = \frac{z_i^2 e_0^2}{8\pi\varepsilon_0 r_i}\left(\frac{1}{\varepsilon_{pore}} - \frac{1}{\varepsilon_f}\right) \tag{9}$$

where e_0 is the electronic charge, ε_0 is the absolute permittivity of vacuum, $\varepsilon_{pore,}\varepsilon_f$ are the relative permittivity of the solvent within the pore and in the bulk feed solution (taken equal to the dielectric constant of pure water) respectively and r_i is the Stokes radius of the solute.

Similarly, the equilibrium boundary condition at the membrane-permeate solution interface is given by

$$\frac{\gamma_{i,pore} C_{i,pore}}{\gamma_{i,p} C_{i,p}} = \Phi_i \Phi_B \exp\left(-\frac{z_i F}{RT}\Delta\psi_{D,p}\right)\Bigg|_{out} \tag{10}$$

In Eq. (10), $C_{i,pore}$ is the concentration at the exit of the pore, just within the membrane and $C_{i,p}$ is the concentration in the permeate solution just outside the membrane [4]. $\Delta\psi_{D,p}$ is the Donnan potential difference between the point just within the pore exit and the solution at the permeate-membrane interface. The activity coefficients are calculated by the Davies equation given by [4].

$$\ln(\gamma_i) = -Az_i^2\left(\frac{I^{1/2}}{1+I^{1/2}} - 0.3I\right) \tag{11}$$

where I is the ionic strength given by

$$I = 0.5\sum z_i^2 C_i \tag{12}$$

and A is a temperature-dependent parameter given by

$$A = \left(\frac{e_0^3 N_A^{1/2}}{\ln(10)\times 4\pi \times 2^{1/2} \times (\varepsilon^3 k_B^3 T^3)^{1/2}}\right) \tag{13}$$

where k_B is the Boltzmann constant, ε is the permittivity of the medium (the value within the pore or in the bulk feed/permeate), N_A is the Avogadro number.

The ENP equation (given by Eq. (1)) and the relevant boundary conditions (given by Eq. (6) and Eq. (10)) are solved numerically for each solute in each cell. Equations (6) and (10) state that the concentration just within the membrane versus that at the contact surface of the membrane and the feed/permeate solution is governed by the steric, Donnan, and dielectric exclusion effects. It is assumed that the membrane element is working under steady state condition and both solute and solvent mass flow rate are conserved in travelling from one cell to the next. Since at steady state, the molar flux of the solute is independent of its position inside the pore, the following relation is valid [4]:

$$j_{i,pore} = C_{i,p} J_w \tag{14}$$

where $C_{i,p}$ is the permeate concentration just outside the membrane at the permeate side [4].

The mass balance of each solute species $'i'$ in the feed channel is given by Eq. (15).

$$d\dot{m}_{i,f} = -C_{i,p} J_w dS \tag{15}$$

where $m_{i,f}$ is the mass of the solute $'i'$ in the feed side of a cell. Similarly, the mass balance of each solute species $'i'$ in the permeate channel is given by Eq. (16).

$$d\dot{m}_{i,p} = C_{i,p} J_w dS \tag{16}$$

On the other hand, the solvent mass balance on the feed side is given by Eq. (17).

$$dQ_f = -J_w dS \tag{17}$$

Similarly, the solvent mass balance on permeate side is given by Eq. (18).

$$dQ_p = J_w dS \tag{18}$$

The DSPM-DE model equations described above (Eq. 1 to 13) are discretized as shown in reference [4] and solved numerically using MATLAB (version R2013b). Equations 14-18 are discretized by the forward differences method. Alongside solving the model equations and getting the velocity and concentration fields, the hydraulic pressure loss along the feed flow direction is determined by the friction factor. The correlation for the friction coefficient in the feed channel of FilmTec membrane element is taken from [28] which was fitted with respect to experimental data.

$$f = \frac{6.23}{\mathrm{Re}^{0.3}} \tag{19}$$

Accordingly, the pressure drop along the feed channel in the feed flow direction is given by Eq. (20).

$$\Delta P_{loss} = -\frac{f}{2}\frac{l}{D_H}\rho_w u_w^{\ 2} \tag{20}$$

where l is the length along the feed channel in the feed flow direction, u_w is the bulk velocity of flow at that location, and D_H is the hydraulic diameter of the feed channel. In a single leaf, the permeate flow rate is low compared to the feed flow rate even at high recovery ratios. Consequently, the permeate Reynolds number is also low and there is no significant hydraulic pressure loss in the permeate channel. Therefore, the hydraulic pressure drop in the permeate channel was not included and the permeate channel was considered to be uniformly at atmospheric pressure.

For the mass transfer coefficient, the expression given by [29] and [30] for spiral wound membranes (which includes the effect of spacers) was used as given by Eq. (21)

$$k_i = 0.753\left(\frac{\eta}{2-\eta}\right)^{1/2}\left(\frac{D_{i,\infty}}{h_f}\right)Sc^{-1/6}\left(\frac{Pe_i}{h_f L_{mix}}\right)^{1/2} \tag{21}$$

where: η is the mixing efficiency of spacer; L_{mix} is the mixing length of the spacer; h_f is the feed channel height; Pe_i is the Peclet number in the channel given by $Pe_i = \frac{2h_f u_w}{D_{i,\infty}}$; and Sc_i is the Schmidt number for each solute species, given by $Sc_i = \frac{\nu}{D_{i,\infty}}$.

Concentration polarization on the feed side is considered by applying a mass balance at the interface between the feed solution and the membrane, as given by Eq. (22) [4]. However, the permeate side concentration polarization is neglected, which is a reasonable assumption for pressure-driven membrane processes such as nanofiltration and reverse osmosis [31], [32], [33].

$$j_i = -k_i(C_{i,m} - C_{i,f}) + J_w C_{i,m} - z_i C_{i,m} D_{i,\infty} \frac{F}{RT}\xi \tag{22}$$

where ξ is the electrical potential gradient at the feed-membrane interface in the continuum phase, just outside the electrical double layer [4].

The transmembrane osmotic pressure is calculated by the Van 't Hoff equation in any cell

$$\Delta\pi = i_v RT(C_m - C_p) \tag{23}$$

where C_m is the salt concentration at the feed-membrane interface, i_v is the Van 't Hoff coefficient, R is the universal gas constant, and T is the absolute temperature.

Finally, the transmembrane solvent flux is calculated from Eq. (24) as shown below:

$$J_w = \Delta P_{net}\left(\frac{r_{pore}^2}{8\nu\rho_w\left(\frac{\Delta x}{A_k}\right)}\right) = ((P_f - P_p) - \Delta\pi)\left(\frac{r_{pore}^2}{8\nu\rho_w\left(\frac{\Delta x}{A_k}\right)}\right) \tag{24}$$

For our simulations, the NF270 membrane manufactured by Dow and FilmTec was considered. Several authors have investigated this membrane and reported experimental results for the rejection ratio at different fluxes. By fitting the experimental data to the DSPM-DE model, it is found that the membrane has an average pore radius of 0.43 nm and an active layer thickness to porosity ratio of ($\Delta x/A_k$) about 1μm [15], [34]. In addition, the pore dielectric constant is 42.2 from fitting with experiments with sodium-chloride [15]. With the exception of the fitting from magnesium-sulphate experimental data, the NF 270 membrane is found to have a pore dielectric constant close to 40 after fitting with several other solutes [15].

In fact, it is seen that for membrane characterization purposes, among the four parameters required to characterize a nanofiltration membrane, namely pore radius (r_{pore}), ratio of the membrane active layer thickness to porosity ($\Delta x / A_k$), pore dielectric constant (ε_{pore}), and membrane volumetric charge density (C_X), the first three parameters can be assumed unique for a given membrane without much error. These three parameters do not change with the solute concentration in the feed, solution pH or the nature of the solute [14], [15]. However, when any of these parameters are fitted with respect to data from different solutes, their fitted values may vary slightly [3], [14], [15]. These values are numerically very close and therefore, an average value is usually taken [15].

The remaining parameter, the membrane volumetric charge density (C_X), depends on the solute and solvent nature, the solute concentration, and the pH of the solution [3], [15], [16]. Therefore, this parameter must be carefully determined for each case investigated. For the present work, the values of pore radius, active layer thickness to porosity ratio, and the pore dielectric constant for NF270 as mentioned previously were taken, and an effective membrane volumetric charge density was fitted to data taken from [35] (see Table 1.2 in this reference). For this, the flow parameters in the present model were adjusted similar to those in [35] and the rejection ratio and recovery ratio from the model are then matched (with those measured in [35]) by adjusting the membrane charge in the model. For instance, for an inlet feed concentration of 2000 ppm sodium-chloride, in order to achieve a recovery ratio of about 10% and mean rejection of sodium-chloride of 80%, an effective membrane charge density of C_X=-45mol/m^3 was fitted. Comparing this value with values fitted by other researchers for FilmTec membranes, it was found that this value is within reasonable limits for the DSPM-DE model [16]. Therefore, a uniform average membrane charge across the entire membrane is assumed in our model using the calibration step discussed above. It is important to note that in reference [16], the variation of the membrane charge density with solute concentration is investigated for NF250 and NF300, showing that the membrane charge density increases linearly and monotonically with the concentration of sodium-chloride and consequently, the rejection ratio increases monotonically. This is verified by [3] where they show the same trend for Desal-DK membrane for both sodium-chloride and magnesium chloride solutions. Further, from our simulations, it is observed that with increasing membrane charge, each of the quantities such as retentate concentration, permeate concentration, rejection ratio, recovery ratio, transmembrane flux and feed flow rates either increase or decrease monotonically. Therefore, if variation of membrane charge across the membrane were included in the simulation, it would fine-tune the results for each of these quantities, but would not affect the trends observed in the study. The values used to characterize the NF-270 membrane for this case are given in Table 1.

Table 1 Values of membrane characterization parameters

Parameter	Value
r_{pore}	0.43 nm
$\Delta x / A_k$	1 μm
ε_{pore}	42.2
C_X	-45 mol/m^3

For the spiral-wound membrane configuration, the conservation equations are modified to allow for variation of various flow parameters and concentration profiles both in the direction of flow of feed as well as in the perpendicular direction, due to the cross-flow of the permeate stream. According to [36], for a spiral-wound leaf, the height of the feed channel is very small which allows the curvature of the channel to be ignored. Thus, the feed channel in a spiral-wound leaf can be modeled as a thin rectangular duct with a height range of 0.5 – 2 mm. In the present model, the feed channel height was fixed at 0.7 mm, the permeate channel height is of 0.3 mm, and each leaf has a dimension of 1m × 1m, which are commonly used values in commercial spiral-wound membranes [28]. For the flat-sheet membrane, we assumed the same dimensions as for the spiral-wound module in order to make their comparison easier. Since the aim of our study is to investigate the effect of different flow parameters on the nanofiltration performance in the two configurations, it is necessary for the two modules to be similar in structure, thereby allowing us to study the difference in performance due to their different flow configurations.

2.2 Model Validation

Referring to the schematic diagram shown in Fig. 1, validation of our model is performed by comparing the performance results at various operating limits. For instance, when the width and length of the leaf are reduced to a few centimeters, the model results from both the flat-sheet and spiral-wound configurations were compared with the experimental measurements conducted at the lab scale using test cells. In this manner, the large membrane leaf was geometrically reduced to a 'small patch' of membrane. At this limit, there is negligible variation of quantities such as feed concentration and rejection ratio along the length and width of the membrane. Excellent agreement with the experimental data presented by [15] is obtained. In this reference, experiments are performed using a cross-flow test cell manufactured by GE Osmonics, using NF270 and NF99HF membranes at their respective isoelectric points (when membrane charge is effectively zero). The comparison of the simulation results at this limit and the experimental data is shown in Fig. 2. In this limit, since the flat-sheet and spiral-wound modules give very similar results, only one set of simulation data is presented for validation.

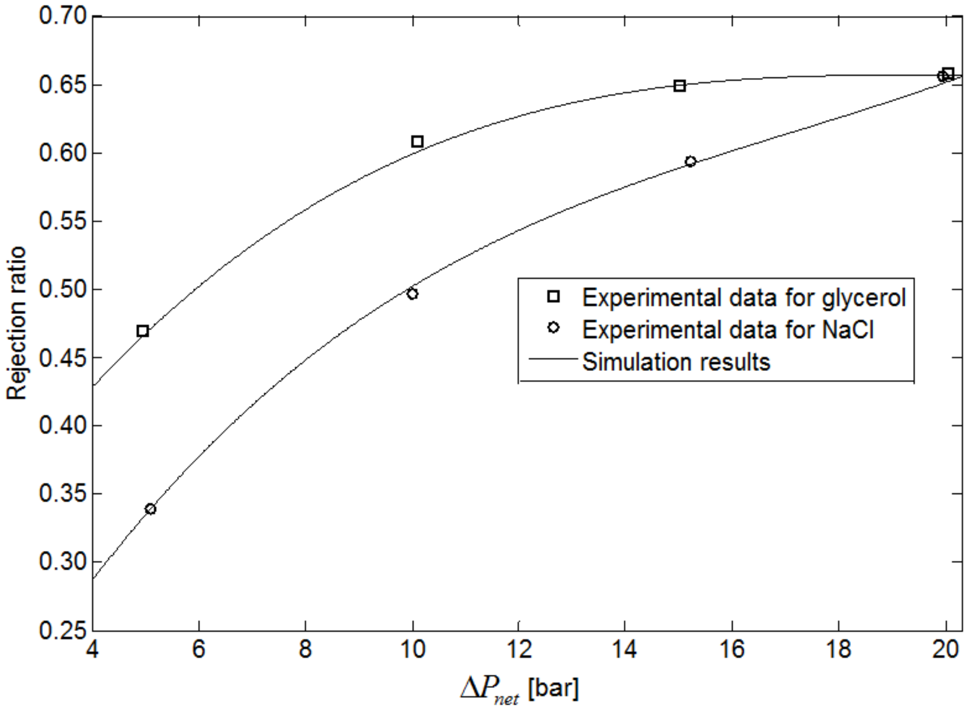

Fig. 2 Comparison between model results and lab-scale experiments for stirred-cell sized membranes [15]

Another validation was conducted with respect to the data provided in Dow technical manual which describes the experimental performance of NF270 membrane under standard test conditions. For the given set of input conditions, the simulation results of the NF270 membrane from the present model are compared with the data provided by Dow [35] using the membrane characteristics shown in Table 1. Our model predicts a recovery ratio of 10% and a mean rejection ratio of 80% for a feed solution of 2000 ppm sodium-chloride as tested and reported in the Dow's manual [35]. These values are in exact agreement with the experimental values reported in Dow manual for the recovery ratio and rejection ratio respectively.

Furthermore, from our model, the characteristic features of the spiral-wound membranes can be observed. These features are in good agreement with the observations found from the detailed modeling study of spiral-wound leaves presented in [17]. Figure 3a, 3b, and 3c show the variations of the trans-membrane pressure (TMP), trans-membrane flux, and feed concentration on the membrane surface respectively. This simulation is conducted at a feed pressure of 1Mpa, feed flow rate of 144 L/h, and an inlet sodium-chloride feed concentration of 2000ppm. It is shown that the maximum values of trans-membrane pressure, trans-membrane flux, and velocity occur at the feed entrance (near the permeate exit side), where the salt concentration is the lowest [17]. This trend is the most prominent for the trans-membrane pressure and to a lesser extent for trans-membrane flux as shown in [17]. In addition, at the diagonally opposite corner of the membrane, at the feed exit (near the permeate entrance) the trans-membrane pressure, trans-membrane flux, and velocity show minimum values where the feed salt concentration is the highest. Figure 3 illustrates the important characteristic traits of a spiral-wound membrane using our model. Exact values of concentration and other quantities at different points on the membrane surface for a nanofiltration spiral-wound membrane were not found in literature which indicates the importance of the present model.

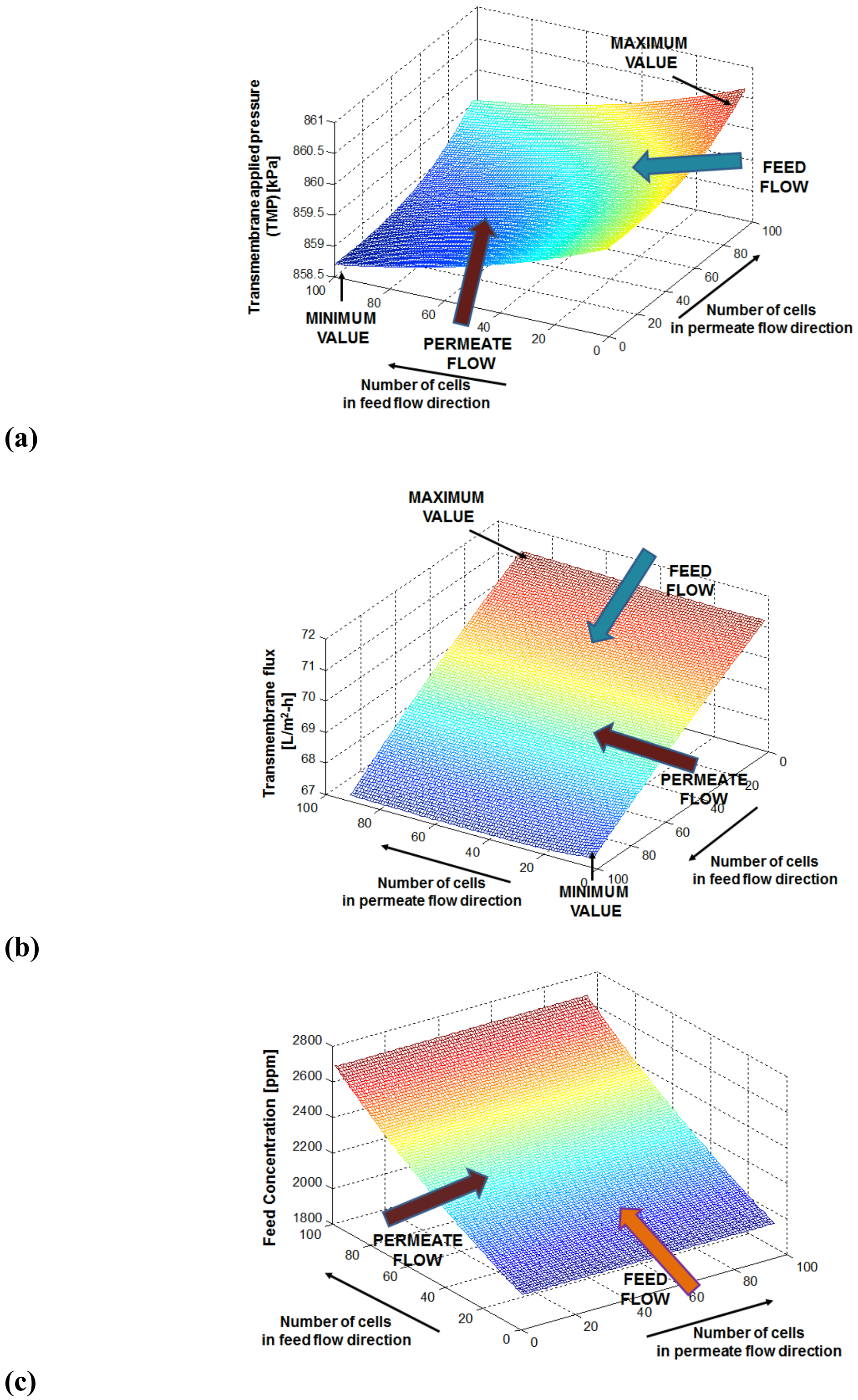

Fig. 3 Variation of the trans-membrane pressure, trans-membrane flux, and feed concentration over the spiral-wound membrane leaf at feed flow rate of 144 L/h and inlet feed pressure of 1 MPa (a) the trans-membrane pressure variation, (b) the trans-membrane flux variation, (c) feed concentration.

3. Results and Discussion

3.1 Analysis of flat-sheet module

In this section, parametric studies are conducted in order to understand the operation of a nanofiltration module and the effect of different flow parameters on its performance. The results presented here are for a 2000 ppm solution of sodium-chloride at 25^{o}C. For the parametric study, a membrane charge of -10.5 mol/m^3 and a pore dielectric constant of 40.4 are considered. These values differ from those is Table 2.1 which provides the parameters used in validation of the model using the NF270 membrane. However, as detailed in section 2.1, the charge of a given membrane is a function of feed operating conditions and so a charge of -10.5 mol/m^3 corresponds to, for example, a feed pH closer to the iso-electric point. Furthemore, it is mentioned in section 2.1 that the NF270 membrane has a pore dielectric constant ~40, as was fitted in reference [15]. Firstly, a single leaf of a flat-sheet membrane as shown in Fig. 1a is considered. The variation of feed and permeate Reynolds numbers along the membrane in the direction of feed flow are fundamental in explaining several other trends, so they are investigated first. The feed Reynolds number decreases along the membrane, since the average bulk flow velocity decreases along the membrane. This results from the decrease in the feed flow volume due to permeation of solution to the permeate side through the membrane. At higher feed flow rates, the feed Reynolds number is greater, as there is greater flow through fixed channel dimensions, causing average bulk flow velocity to be higher. The permeate Reynolds number increases along the membrane, due to the increase in permeate flow rate as a result of the flux entering through the membrane. According to Vitor *et al.* [36] for rectangular channels, the transition between laminar and turbulent flow occurs at a Reynolds number between 150 and 300 in the presence of spacers. In our work, operation over a large range of feed Reynolds number is shown. For instance, at the minimum feed flow rate of 60 L/h per leaf, the feed Reynolds number at the inlet is 50, while for the maximum feed flowrate of 1000 L/h per leaf, the Reynolds number at the inlet is 600.

Figure 4 shows the variation of the feed pressure along the membrane length. The feed pressure decreases along the membrane in the feed flow direction due to hydraulic losses. At higher flow rates and hence higher feed Reynolds numbers, the hydraulic losses are greater due to greater average velocity in the feed channel. Thus, the pressure variation lines slope down at greater angles for greater flow rates. On the other hand, the permeate Reynolds number is maximum at the permeate exit, since the flux permeated through the entire membrane adds up at that point. However, the maximum value of permeate Reynolds number does not exceed 20 at any of the feed flow rates investigated. Thus, due to the very low permeate Reynolds numbers, the hydraulic losses are insignificant and permeate hydraulic pressure remains essentially uniform along the flow direction. Therefore, the trans-membrane hydraulic pressure (TMP) is essentially a sole function of the feed pressure.

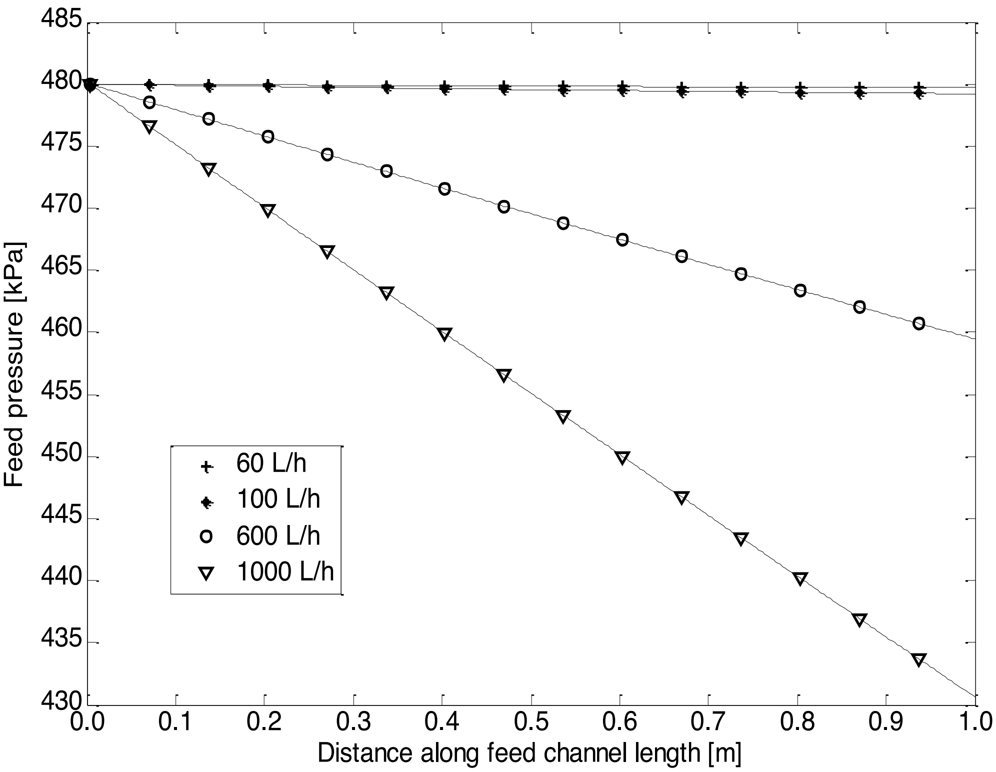

Fig. 4 Feed pressure variation along the feed flow direction at 480 kPa inlet feed pressure and different feed flow rates.

The variation of the solute mass transfer coefficient in the feed channel with respect to feed flow rate is essential in describing the concentration polarization at different flow rates. Its value is proportional to the feed Reynolds number values, and thus at higher Reynolds numbers, the concentration boundary layer is thinner, resulting in lower concentration polarization. Figure 5a and 5b show the variations of the bulk feed concentration at different feed flow rates and feed inlet pressures respectively. Figure 6 shows the concentration at the membrane surface at different feed flow rates. It is noticed in Figs 5 and 6 that at the lowest feed flow rates there is a steep increase of the feed concentration and the concentration at the membrane surface in the flow direction. This is because the Reynolds number decreases to a small value along the feed channel as a result of a low mass flow rate, which also leads to a low mass transfer coefficient, so there is greater concentration polarization. Since at higher values of Reynolds number, there is the combined effect of the higher bulk solute mass flow rate in the feed channel together with the increased transport from the membrane to the bulk of the feed (lower concentration polarization), very little solute enters the permeate channels. This is evident from Fig. 7, which clearly shows that the permeate concentration decreases at higher feed flow rates. Due to the inverse argument, the permeate concentration increases along the membrane due to the decreasing feed Reynolds numbers.

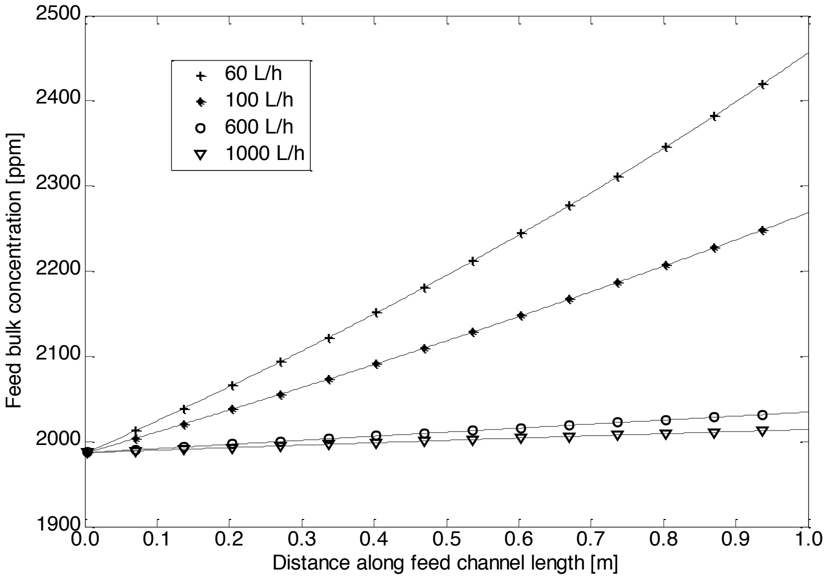

(a)

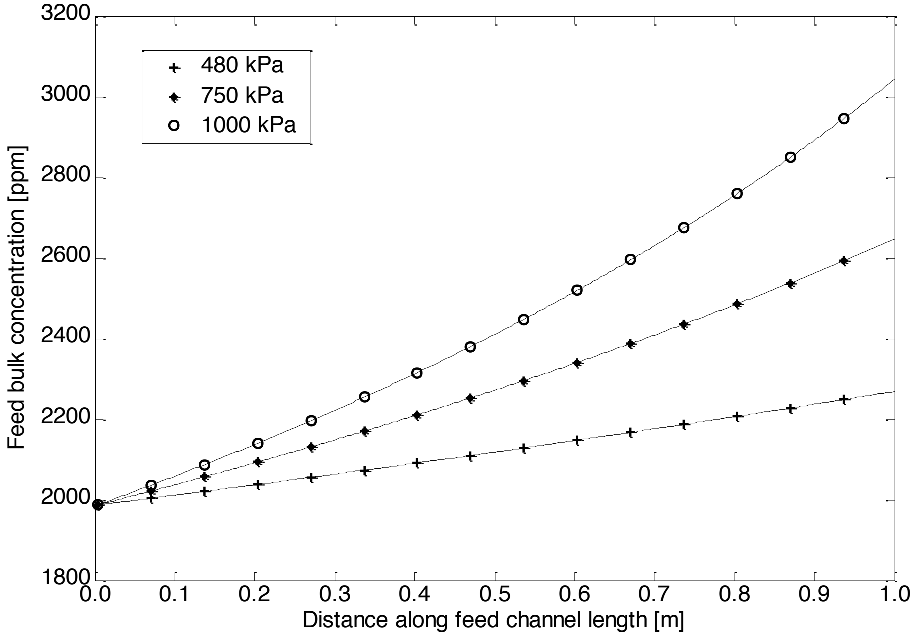

(b)

Fig. 5 Variation of feed bulk concentration along feed flow direction at (a) 480 kPa inlet feed pressure and different feed flow rates, and (b) 100 L/h flow rate and different feed inlet pressures.

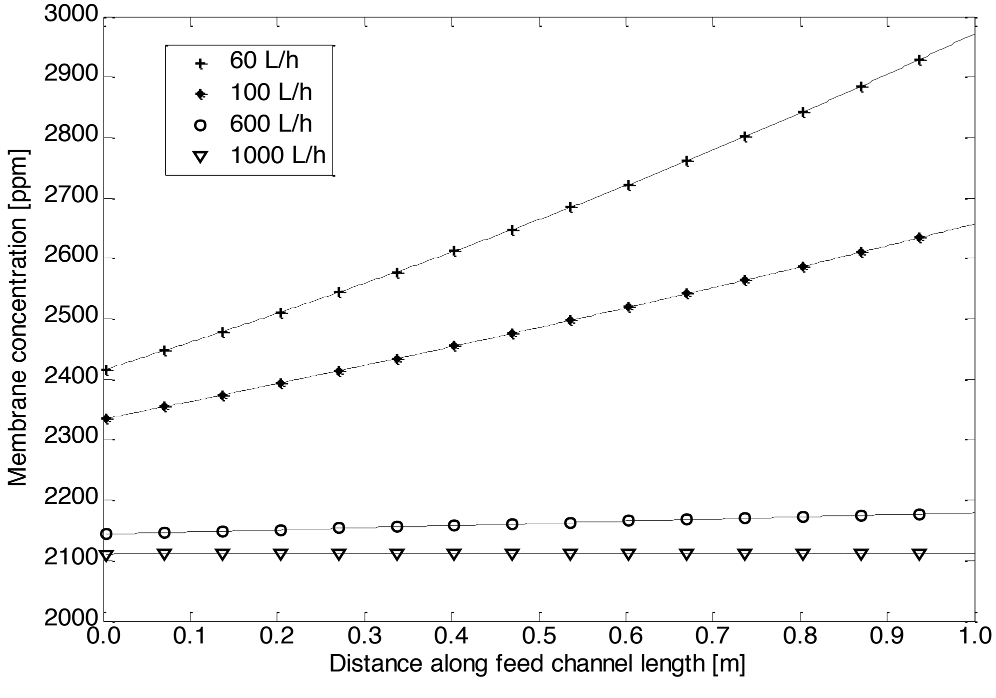

Fig. 6 Variation of the feed concentration at membrane surface on feed side along the feed flow direction at 480 kPa inlet feed pressure and different feed flow rates.

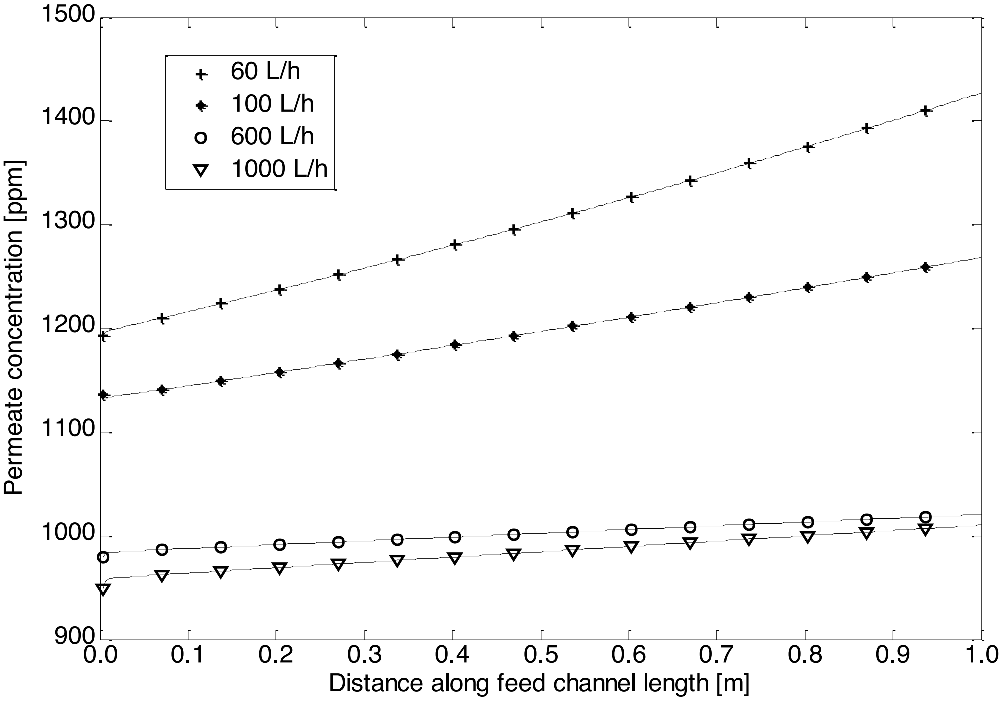

Fig. 7 Variation of permeate concentration along feed flow direction at 480 kPa inlet feed pressure and different feed flow rates.

The trans-membrane osmotic pressure, as given by Eq. (23) follows the trend of the membrane concentration, since the variation of permeate concentration along the channel is relatively small. For a given feed pressure, the net driving pressure, defined in Eq. (24) as $\Delta P_{net} = ((P_f - P_p) - \Delta\pi)$, first increases with the flow rate and then decreases (see Fig. 8a). This is because initially, at lower feed flow rates, the feed pressure dominates over the trans-membrane osmotic pressure, resulting in high net driving pressure. However, with increasing feed flow rates, the increased hydraulic losses cause the feed pressure to decrease rapidly along the feed flow direction. Thus, the effect of the trans-membrane osmotic pressure is more prominent at higher feed flow rates and the net driving force is decreased. Further appreciation of this trend of variation of net driving pressure can be obtained by observing its variation at any fixed point of the membrane with respect to flow rate. The net driving pressure at the mid-point of the membrane at different flow rates is shown in Fig. 8b. It is to be noted that the flow rate at which the net driving pressure is maximum will be different if a different inlet feed concentration is considered or different membrane properties are considered but the trend of variation with flow rate will be similar. Since the trans-membrane flux is directly dependent on the driving force, the variation of the trans-membrane flux is exactly similar to the driving force as clearly illustrated in Fig. 9.

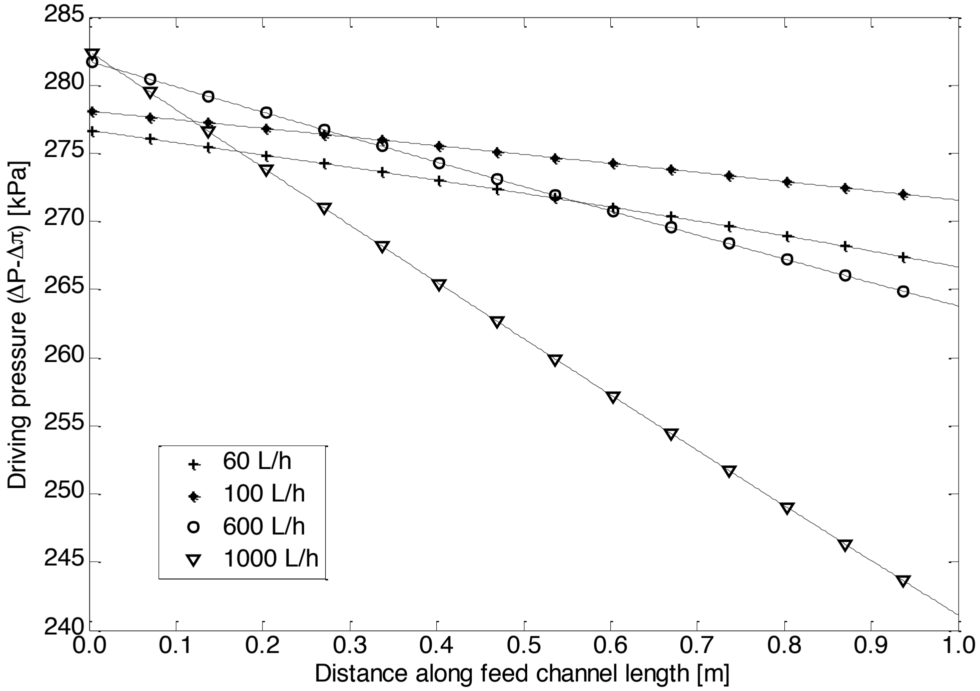

(a)

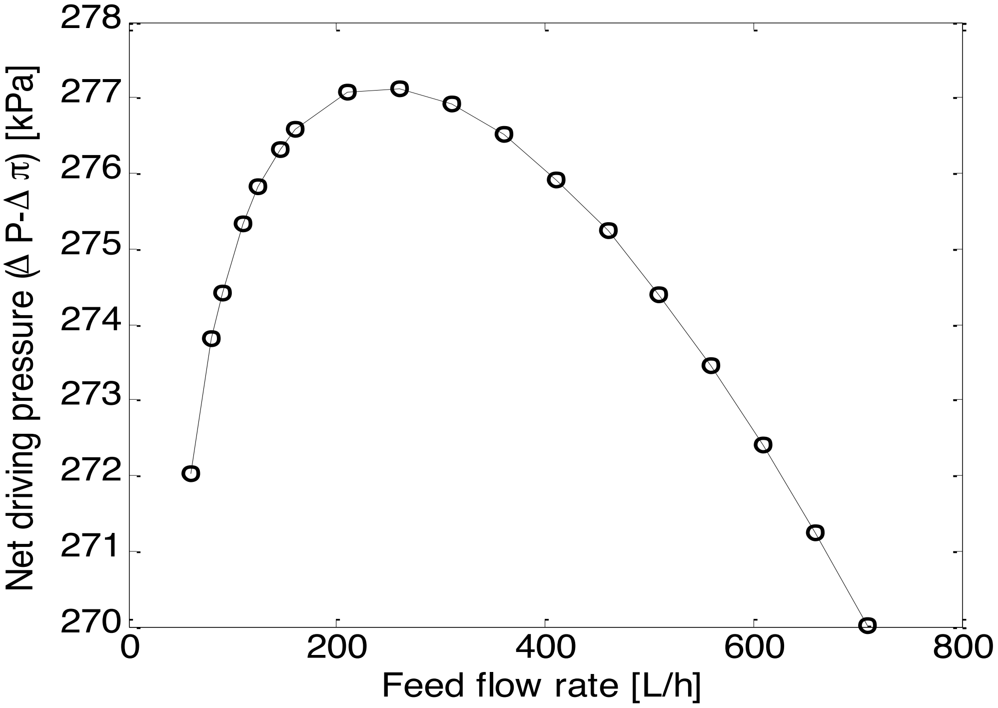

(b)

Fig. 8 Driving pressure at 480 kPa inlet feed pressure and different flow rates (a) variation along the membrane length, (b) at midpoint of the feed channel

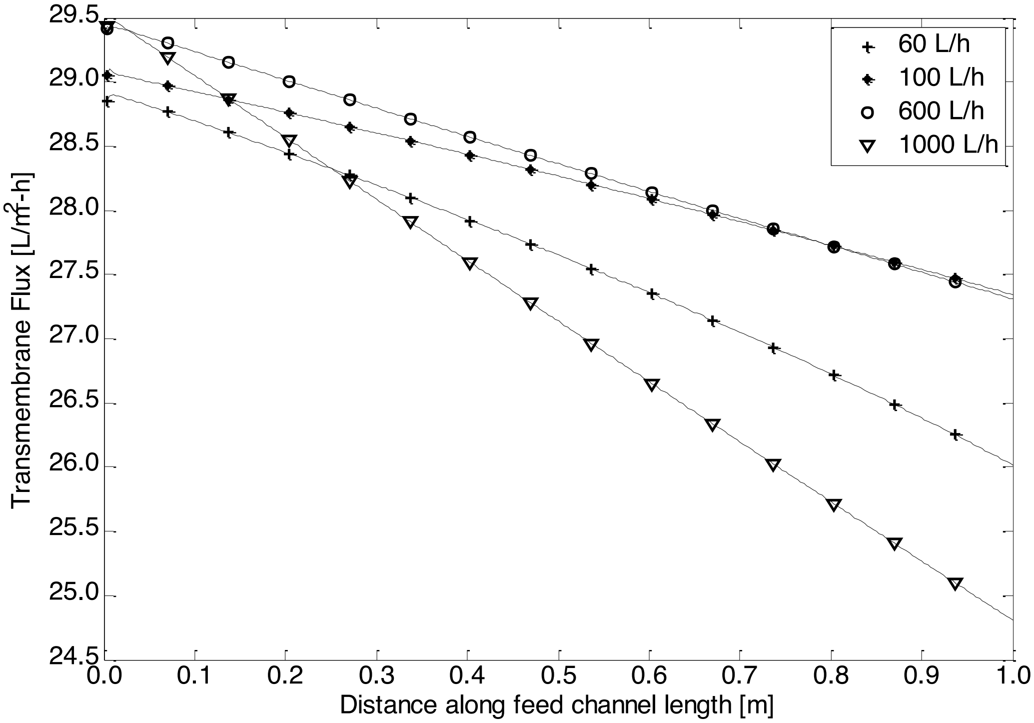

Fig. 9 Variation of transmembrane flux along feed flow direction at 480 kPa inlet feed pressure and different feed flow rates.

Figure 10 shows the variation of the overall rejection ratio of the membrane with feed pressure and feed flow rate. It is illustrated that the rejection ratio increases monotonically with the feed pressure. This is because the driving force is higher, causing solvent permeation to be higher, therefore 'leaving behind' the solute ions. On the other hand, the rejection ratio increases with the flow rate but reaches an asymptotic value. This is because when increasing the flow rate, initially the driving force and hence the solvent permeation increases but as the flow rate is further increased, the driving force is decreased (due to the role of hydraulic pressure losses), causing lower solvent flux and hence decreased rejection. Figure 11 shows the variation of the net recovery ratio with flow rate, at different feed pressures. As shown in this figure, at higher flow rates, the recovery ratio decreases. This is because the net driving pressure decreases, causing a decrease in the trans-membrane flux. Since the permeate flow is created by the flux coming in from the feed side, the decreased trans-membrane flux implies a reduced recovery ratio. Similarly, the recovery ratio increases with the feed pressure because the driving force for permeation increases causing a greater trans-membrane flux and hence greater recovery.

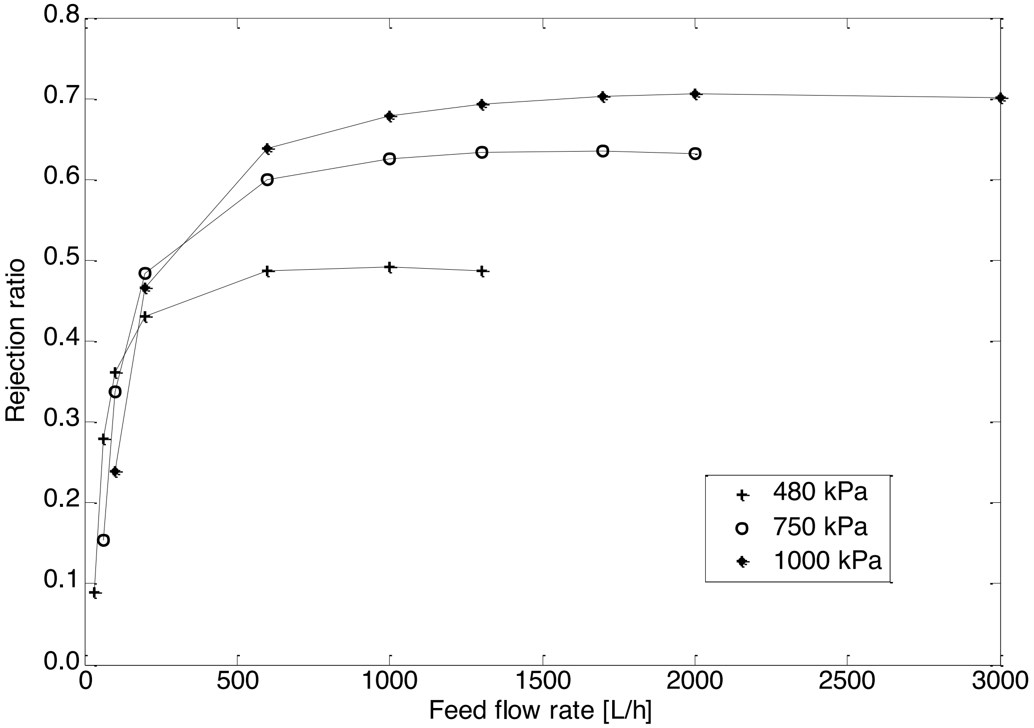

Fig. 10 Rejection ratio for NaCl at different feed flow rates and inlet feed pressures.

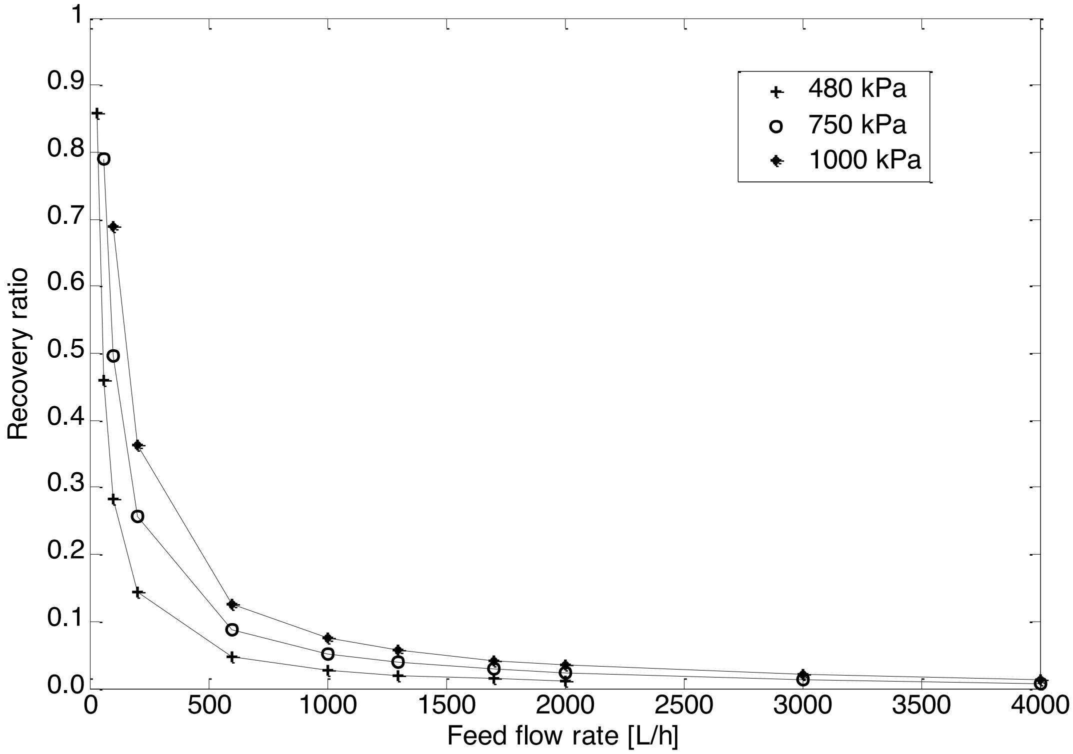

Fig. 11 Recovery ratio at different feed flow rates and inlet feed pressures.

3.2 Analysis of spiral-wound module

The operation of the spiral-wound membrane can be explained similarly to that of the flat-plate configuration. The trends of variation of quantities such as the Reynolds numbers, mass transfer coefficients, feed concentrations, rejection ratios and recovery ratio with respect to feed flow rate and feed pressure are similar to the flat-sheet case. The key difference is that in the spiral-wound module, these quantities also vary in the permeate-flow direction, perpendicular to the feed flow. To compare the performance of the spiral-wound membrane with the flat-sheet, Fig. 12 shows surface plots of the trans-membrane hydraulic pressure (TMP), trans-membrane flux and rejection ratio in the two configurations under similar operating conditions (i.e. flow rate of 250 L/h, feed inlet pressure of 480 kPa, and inlet feed concentration of 2000 ppm sodium-chloride). The spiral-wound membrane shows the maximum and minimum values of the TMP and flux at opposite corners of the membrane. The range of the three quantities plotted is similar in both the flat-sheet and spiral-wound membranes. Therefore, for identical leaf geometry and identical flow conditions, the flat-sheet and spiral-wound configurations give similar results. Since the computational model for the flat-sheet membrane is computationally less time consuming and less complex compared with the spiral-wound configuration, it would be advantageous to use the flat-sheet configuration model instead of the spiral-wound one without losing significant information.

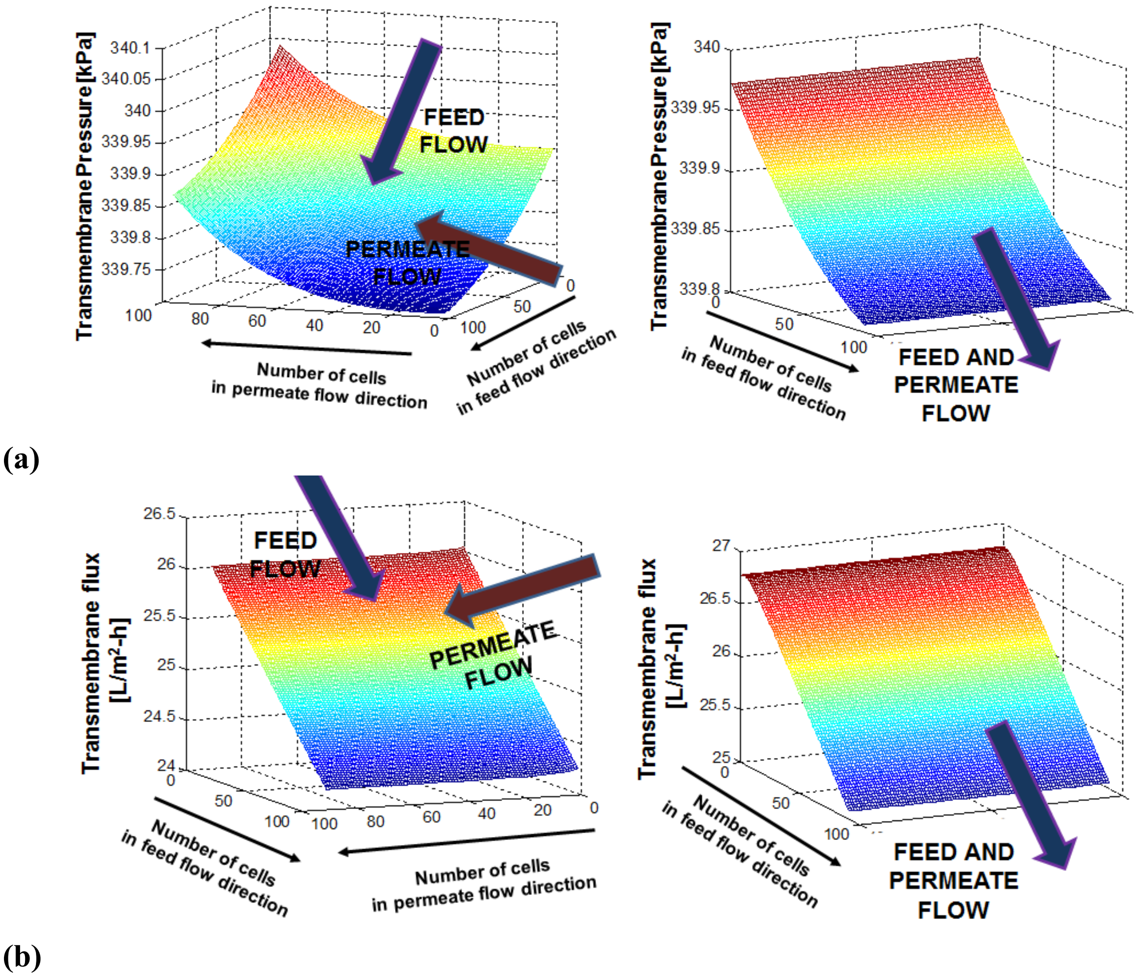

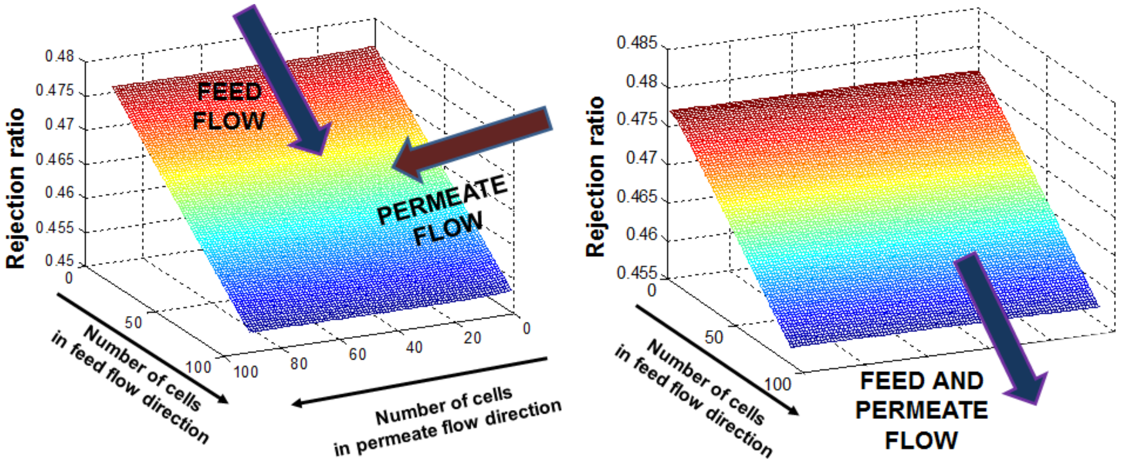

(c)

Fig. 12 Comparison of values for spiral-wound membrane and flat-sheet membrane at 250 L/h feed flow rate and 480 kPa feed pressure: (a) trans-membrane pressure (TMP), (b) trans-membrane flux, and (c) rejection ratio.

To investigate this further, it is necessary to check if under different flow conditions, the variation of quantities in the permeate flow direction is significant. Four flow rates spread over a wide range, 1805 L/h, 361L/h, 110 L/h and 50L/h were investigated at different values of feed inlet pressures (480 kPa, 750 kPa and 1000kPa) and 2000 ppm sodium-chloride solution was considered. It was observed that the variation of the feed flow rate, net driving pressure, trans-membrane flux, rejection ratio, and feed concentration in the direction of permeate flow (percentage variation from beginning of permeate flow to the permeate exit) is less than 10 % in all cases and less than 5% in most cases. The only quantity that shows marked variation along the permeate flow direction is the permeate Reynolds number which has a maximum value of about 20 at the feed entrance, near the permeate exit. It is close to zero along the edge of the leaf where the permeate flow begins.

Therefore, it can be concluded that for similar geometric specifications, the computationally less intensive flat-sheet model introduced in this work can be used to predict the performance of the spiral-wound membrane. This observation is especially helpful for the investigation of large scale-systems where series of spiral-wound membrane elements are used. Since in a membrane element the spiral-wound leaves are in parallel, the rejection ratio and recovery ratio for the entire element is the same as that of the individual leaf. In order to model a series of elements, the modeling can be simply made so that the exit feed flow rate and pressure will be the inlet values for the next element.

3.3 Seawater Nanofiltration

The model of nanofiltration introduced in this work is now applied to seawater and it is validated with respect to a large scale desalination system, the Umm Lujj NF-SWRO plant owned by the Saline Water Conversion Corporation, Research and Development Center (SWCC-RDC) [37], [38]. Gulf seawater concentration [23], as shown in Table 2, is used as the initial feed solution. The setup of the Umm Lujj NF unit described in the references is modeled, and it is attempted to match the overall recovery ratio and rejection ratio for each individual ion when the flow conditions as specified in [37] are applied. The nanofiltration unit of the desalination plant described in references [37] and [38], consists of several pressure vessels in parallel. Each vessel consists of six spiral-wound elements of the DK8040F membrane manufactured by GE-Osmonics, in series. Since the pressure vessels operate in parallel, the rejection ratio and recovery ratio of the entire NF unit is represented by the values obtained for a single vessel. In order to model a pressure vessel, six elements are modeled such that the exit feed pressure and flow rate from each element is the inlet for the next element. The inlet feed pressure and inlet feed flow rates are taken as 30 bar and 13.3 m^3/h respectively, which are the values given for each vessel in [37]. The recovery ratio in each vessel in reference [37] was found to be 65%.

Table 2 Validation of solute rejection ratios from model for sea-water nanofiltration in a large scale desalination plant

Ion	Concentration in seawater (ppm)	Rejection ratio [37]	Rejection ratio from present model	% Deviation
Ca^{2+}	491	91	90.65	0.384
Mg^{2+}	1556	98	99.39	-1.41
SO_4^{2-}	3309	99.9	93.50	6.40
Cl^-	23838	24	27.73	-15.54
HCO_3^-	155.5	56	49.44	11.71

Since the NF unit described in the Umm Lujj plant [37] [38] uses DK8040F membrane which falls under the broad category of Desal-DK membranes manufactured by GE-Osmonics, it is necessary to obtain the membrane characteristics which give a good fit with the DSPM-DE model. In this simulation, the results from the characterization of Desal-DK membranes given in references [1], [3]are used. They found the pore radius to be 0.45 nm and the active layer thickness to porosity ratio ($\Delta x / A_k$) to be 3μm (when characterized by glucose). The pore dielectric constant is found to be 38. However, in order to obtain good correspondence with the data in [37], values of pore dielectric constant and membrane charge density are set to ε_{pore} = 56.5 and $C_X = -80$ mol/m^3. The deviation of the pore dielectric constant from the value in literature may be due to the fact that in the references, the fitting is done with respect to the rejection data of a single solute such as sodium-chloride, whereas in seawater there is a mixture of ions, each of which has its own unique behavior with the membrane. The interaction of different solutes with the same membrane can indeed be very different. For example, in [15] (Table 4), it is found that the dielectric constant of the membranes NF99HF and NF270 is around 40 from characterization with respect to sodium-chloride, potassium-chloride, and sodium-sulphate, while magnesium-sulphate, gives a value around 75 for NF99HF and 65 for NF270, thereby indicating that this salt has a unique chemistry with the membrane [15]. In addition, in [16] (Table 2), it is seen that characterization of volumetric charge density for the both the membranes NF300 and NF250 with respect to sodium-chloride give negative values, while fitting with respect to magnesium-chloride gives a positive membrane charge density. Since seawater contains not only sodium, chloride, sulphate, and magnesium ions, but also several other ions, it is expected that the final values of the pore dielectric constant and membrane charge to be an 'average' value that represents the interaction of all these ions with the membrane.

Furthermore, the membrane charge density changes with solute concentration and therefore will vary from element to element in the series. However, in order to find a relation for the variation of membrane charge density as a function of feed concentration (by the method demonstrated in reference [16]) for seawater, a few experiments need to be performed, which is beyond the scope of our research thus far. As mentioned previously, a simple correlation between solute concentration and membrane charge density can be obtained from experimental analysis. However, for seawater the situation is made more complex by the fact that it contains a variety of solute ions and the type of correlation varies from solute to solute. For example, in [39], the charge-concentration correlation for calcium-chloride is found to be almost parabolic while that for sodium-chloride is linear. Therefore, to simplify the situation, the same value of membrane charge density for all the six elements is taken for the simulation.

As mentioned earlier, even though a charge density for all the elements in series is considered, which is not completely rigorous, the present model is able to predict the relative values of rejection of each ion with respect to the others correctly; and, for the flow parameters used in the Umm Lujj plant, the model is able to correctly predict the recovery ratio. Further experimentation to correlate seawater concentration with membrane charge will fine-tune the values of rejection ratio of each ion and improve the agreement with experimental values. As observed in the Table 2, there is a good agreement of values and trends with the reference. A recovery ratio of 65.41% for each vessel is obtained by the simulation, which has an error of only 0.63% with respect to the reference. Thus our model can be used with confidence in the modeling of seawater nanofiltration.

4. Conclusions

In this work comprehensive models for large-scale nanofiltration using the flat-sheet and spiral-wound configurations are developed by extending the DSPM-DE model over a membrane leaf. The models for the individual leaves can be easily extended to put them in series or parallel, in order to simulate membrane modules and trains of modules, as one would find in desalination plants. The effects of flow parameters such as feed pressure and flow rate on the solute rejection and recovery ratio of the membrane have been investigated. The variation of other quantities such as feed concentration, permeate concentration and trans-membrane flux over the leaf have also been presented. These studies have shown that the rejection and recovery ratios of the NF membrane ultimately depend on the net driving pressure across the membrane. An analysis of how the driving pressure is affected by the feed flow conditions is made. It is shown that the net driving pressure increases with feed pressure. It increases with increase in feed flow rate until hydraulic pressure losses become dominant.

The two configurations modeled (flat-sheet and spiral-wound) are distinguished by the feed and permeate flow arrangements. In flat-sheet modules, the feed and permeate flows in their respective channels are parallel to each other, while in the spiral-wound case, the feed and permeate flow are perpendicular to one-another. Our work shows that for similar geometric properties, under similar operating conditions, the spiral-wound and flat-sheet configurations perform similarly. This observation is significant because although the spiral-wound configuration is commercially more common, it is computationally more expensive and complicated. The ability of the flat-sheet model to predict the performance of the spiral-wound configuration greatly reduces the computational expense.

Our work also shows that for reasonable values of fit of membrane characterization parameters with respect to the DSPM-DE model, the performance of nanofiltration membranes for seawater desalination can be accurately predicted. This is established by validating the model with results from a large-scale desalination plant. The establishment of the model as a reliable means to simulate the performance of nanofiltration in large-scale systems opens up doors for the investigation of NF in several processes, over a wide range of operating conditions, whether it is in a desalination system or in any of several other applications, thereby reducing dependence on experimental data.

Further work is needed, however to characterize how membrane charge density varies with concentration of seawater. This will give a more accurate prediction of seawater nanofiltration when several membrane elements are in series. Membrane charge characterization as a function of concentration will require experiments to fit the charge density for different ratios of seawater ions to water in solution, which can then be tied together by a relation obtained by fitting to get membrane charges over a large range of concentrations.

Acknowledgments

The authors would like to thank King Fahd University of Petroleum and Minerals in Dhahran, Saudi Arabia, for funding the research reported in this paper through the Center for Clean Water and Clean Energy at MIT and KFUPM. In addition, Yagnaseni Roy would like to thank Leonardo D. Banchik immensely for his continuous support and technical advice.

References

[1] W. R. Bowen and J. S. Welfoot, "Modelling of membrane nanofiltration—pore size distribution effects," *Chemical Engineering Science,* vol. 57, no. 8, p. 1393 – 1407, 2002.

[2] N. Hilal, H. Al-Zoub, N. A. Darwish, A. W. Mohammad and M. Abu Arabi, "A comprehensive review of nanofiltration membranes: Treatment, pretreatment, modelling, and atomic force microscopy," *Desalination,* vol. 170, pp. 281-308, 2004.

[3] W. R. Bowen and J. S. Welfoot, "Modelling the performance of membrane nanofiltration—critical assessment and model development," *Chemical Engineering Science,* vol. 57, p. 1121 – 1137, 2002.

[4] V. Geraldes and A. M. Brites Alves, "Computer program for simulation of mass transport in nanofiltration membranes," *Journal of Membrane Science,* vol. 321, p. 172–182, 2008.

[5] S. Bandini and D. Vezzani, "Nano¬filtration modeling: the role of dielectric exclusion in membrane characterization," *Chemical Engineering Science,* vol. 58, p. 3303 – 3326, 2003.

[6] R. Rautenbach and A. Groschl, "Separation Potential of Nanofiltration Membranes," *Desalination,* vol. 77, pp. 73-84, 1990.

[7] W. Jin, A. Toutianoush and B. Tieke, "Use of Polyelectrolyte Layer-by-Layer Assemblies as Nanofiltration and Reverse Osmosis Membranes," *Langmuir,* vol. 19, pp. 2550-2553, 2003.

[8] P. Eriksson, "Nanofiltration Extends the Range of Membrane Filtration," *Environmental Progress,* vol. 7, pp. 58-62, 1988.

[9] A. I. Schäfer, A. G. Fane and T. D. Waite, Nanofiltration : Principles and Applications, Oxford,UK; New York, NY: Elsevier, 2005.

[10] R. Rautenbach, K. Vossenkaul, T. Linn and T. Katz, "Waste water treatment by membrane processes - New development in ultrafiltration, nanofiltration and reverse osmosis," *Desalination,* vol. 108, pp. 247-253, 1996.

[11] W. R. Bowen and A. W. Mohammad, "Diafiltration by Nanofiltration: Prediction and Optimization," *AIChE Journal,* vol. 44, no. 8, pp. 1799-1812, 1998.

[12] A. A. Hussain and A. E. Al-Rawajfeh, "Recent Patents of Nanofiltration Applications in Oil Processing, Desalination,Wastewater and Food Industries," *Recent Patents on Chemical Engineering,* vol. 2, pp. 51-66, 2009.

[13] A. E. Al-Rawajfeh, H. E. S. Fath and A. A. Mabrouk, "Integrated Salts Precipitation and Nano-Filtration as Pretreatment of Multistage Flash Desalination System," *Heat Transfer Engineering,* vol. 33, pp. 272-279, 2012.

[14] W. R. Bowen and A. W. Mohammad, "Characterization and prediction of Nanofiltration membrane performance a General assessment," *Trans IChemE,* vol. 76, pp. 885-893, 1998.

[15] D. L. Oatley, L. Llenas, R. Pérez, P. M. Williams, X. Martínez-Lladó and M. Rovira, "Review of the dielectric properties of nanofiltration membranes and verification of the single oriented layer approximation," *Advances in Colloid and Interface Science,* vol. 173, p. 1–11, 2012.

[16] N. S. Kotrappanavar, A. A. Hussain, M. E. E. Abashar, I. S. Al-Mutaz, T. M. Aminabhavi and M. N. Nadagouda, "Prediction of physical properties of nanofiltration membranes for neutral and," *Desalination,* vol. 280, p. 174–182, 2011.

[17] J. Schwinge, P. R. Neal, D. E. Wiley, D. F. Fletcher and A. G. Fane, "Spiral wound modules and spacers Review and analysis," *Journal of Membrane Science,* vol. 242, p. 129–153, 2004.

[18] N. Hilal, H. Al-Zoub, A. W. Mohammad and N. A. Darwish, "Nanofiltration of highly concentrated salt solutions up to seawater salinity," *Desalination,* vol. 184, p. 315–326, 2005.

[19] K. H. Mistry and J. H. Lienhard V, "Effect of nonideal solution behavior on desalination of a sodium chloride (NaCl)solution and comparison to seawater," *Journal of Energy Resources Technology,* vol. 135, 2013.

[20] K. H. Mistry, H. A. Hunter and J. H. Lienhard V, "Effect of composition and nonideal solution behavior on desalination calculations for mixed electrolyte solutions with comparison to seawater," *Desalination,* vol. 318, p. 34–47, 2013.

[21] M. A. K. AI-Sofi, A. M. Hassan, G. M. Mustafa, A. G. I. Dalvi and M. N. M. Kither, "Nanofiltration as a means of achieving higher TBT of > 120°C in MSF," *Desalination,* vol. 118, pp. 123-129, 1998.

[22] M. A. K. Al-Sofi, "Fouling phenomena in multi stage flash (MSF) distillers," *Desalination,* vol. 126, pp. 61-76, 1999.

[23] O. A. Hamed, A. M. Hassan, K. Al-Shail and M. A. Farooque, "Performance analysis of a trihybrid NF/RO/MSF desalination plant," *Desalination and Water Treatment,* vol. 1, p. 215–222, 2009.

[24] C. O. Anne, D. Trebouet, P. Jaouen and F. Quemeneur, "Nanofiltration of seawater: fractionation of mono and multi-valent cations," *Desalination,* vol. 140, pp. 67-77, 2001.

[25] C. J. Harrison, Y. A. Le Gouellec, R. C. Cheng and A. E. Childress, "Bench-Scale Testing of Nanofiltration for Seawater Desalination," *J. Environ. Eng,* vol. 133, pp. 1004-1014, 2007.

[26] J. L. Andersen and J. A. Quinn, "Restricted Transport in Small Pores A Model for Steric Exclusion and Hindered Particle motion," *Biophysical Journal,* vol. 14, pp. 130-150, 1974.

[27] M. G. Davidsom and W. M. Deen, "Hydrodynamic Theory for the Hindered Transport of Flexible Macromolecules In Porous Membranes," *Journal of Membrane Science,* vol. 35, pp. 167-192, 1988.

[28] G. Schock and A. Miquel, "Mass transfer and pressure loss in spiral wound modules," *Desalination,* vol. 64, pp. 339-352, 1987.

[29] S. Senthilmurugan, A. Ahluwalia and S. K. Gupta, "Modeling of a spiral-wound module and estimation of model parameters using numerical techniques," *Desalination,* vol. 173, pp. 269-286, 2005.

[30] F. Evangelista, "An Improved Analytical Method for the Design of Spiral-wound modules," *The Chemical Engineering Journal,* vol. 38, p. 33 – 40, 1988.

[31] E. Nagy, E. Kulcsar and A. Nagy, "Membrane mass transport by nanofiltration: Coupled effect of the polarization and membrane layers," *Journal of Membrane Science,* vol. 368, p. 215–222, 2011.

[32] R. J. McCutcheon and M. Elimelech, "Influence of concentrative and dilutive internal concentration polarization on flux behavior in forward osmosis," *Journal of Membrane Science,* vol. 284, p. 237–247, 2006.

[33] R. Rautenbach and F. Helmus, "Some considerations on mass-transfer resistances in solution-diffusion-type membrane processes," *Journal of Membrane Science,* vol. 87, pp. 171-181, 1994.

[34] M. Dalwania, N. E. Benes, G. Bargeman, D. Stamatialis and M. Wessling, "Effect of pH on the performance of polyamide/polyacrylonitrile based thin film composite membranes," *Journal of Membrane Science,* vol. 372, p. 228–238, 2011.

[35] "Dow Water & Process Solutions FILMTEC™ Reverse Osmosis Membranes Technical Manual.".

[36] V. Geraldes, V. Semiao and M. N. de Pinho, "Flow management in nanofiltration spiral wound modules with ladder-type spacers," *Journal of Membrane Science,* vol. 203, p. 87–102, 2002.

[37] A. M. Hassan, M. Al-Sofi, A. M. Al-Ajlan, A. Al-Azzaz and A. Al-Mohammadi, "The New NF-SWRO Operation Increased Significantly UmmLujj SWRO Plant Output and Recovery".

[38] A. A. Al-Hajouri, A. S. Al-Amoudi and A. ,. M. Farooque, "Long term experience in the operation of nanofiltration pretreatment unit for seawater desalination at SWCC SWRO plant," *Desalination and Water Treatment,* vol. 51, p. 1861–1873, 2013.

[39] C. Mazzoni, L. Bruni and S. Bandini, "Nanofiltration: Role of the Electrolyte and pH on Desal DK Performances," *Industrial & Engineering Chemistry Research,* vol. 46, pp. 2254-2262, 2007.